PAPER

Check for updates

Iron oxide nanocube assembly on silver nanowire templates to enhance magnetic hyperthermia performance

Tugce A. Arica, [a,b] Ecem Tiryaki, [b] Ehsan Sadeghi, [b,c] Abubakar R. Mannir, [b] Sinan Balci [ID] [d] and Teresa Pellegrino [ID] *[b]

Iron oxide nanocubes (IONCs) represent one of the benchmark magnetic nanoparticles able to most efficiently convert magnetic energy into heat for magnetic hyperthermia cancer treatment, and their heat losses can be further increased by controlling their assembly through the synthesis of ordered structures. However, achieving the alignment of nanoparticles with one-dimensional chain or columnar structures into long arrays to then study their magnetic heat losses still remains a significant challenge. This study exploits silver nanowires as high-surface-area anisotropic templates for the controlled chaining of IONCs. The surfaces of the IONCs were purposely functionalized with polyethyleneimine (IONCs@PEI) and interacted with silver nanowire (AgNW) surfaces *via* electrostatic attraction. Here, alternating current (AC) magnetometry was employed to compare the heating performance expressed as specific absorption rate values between individually coated IONCs@PEI and AgNWs@IONCs@PEI composites at various magnetic field strengths and frequencies. SAR values reveal that clustering of IONCs on AgNW surfaces improves the heating efficiency at an applied magnetic field strength of 24 kA m^{-1}, regardless of the applied frequencies, with SAR values of AgNWs@IONCs@PEI composites outperforming those of individual IONCs@PEI. Moreover, dynamic hysteresis loops showed that the coercive field of AgNWs@IONCs@PEI increased significantly at 24 kA m^{-1}, indicating the existence of strong magnetic dipolar interactions between nanoparticles. This study shows an innovative approach for guiding the orientation of magnetic nanoparticles using one-dimensional templates to enhance their heating performance.

Introduction

Magnetic hyperthermia therapy (MHT) is a promising cancer treatment approach that uses magnetic nanoparticles to generate heat inside tumors.[1–3] The nanoparticles delivered to the tumor site dissipate heat under an externally applied AC magnetic field, which raises the tumor temperature from 37 °C to a therapeutic range of 42–46 °C, causing damage to cancer cells by various mechanisms. In some other examples, MHT can also induce non-thermal effects like mechanical damage, localized heat cell membrane damage, and reactive oxygen species (ROS) production.[4,5] The heating performance of the magnetic nanoparticles is quantified using the specific absorption rate (SAR), which determines the rate at which a magnetic material absorbs electromagnetic energy and converts it into heat. To minimize the required particles for MHT and keep the applied magnetic field at clinically acceptable levels, the SAR should attain the highest possible value.[6]

Magnetic nanoparticles' dynamic magnetization response is the basis for calculating the SAR. The effective magnetic anisotropy of nanoparticles together with other MNP parameters, including the magnetic volume, saturation of magnetization, hydrodynamic size, as well as the frequency and amplitude of the external magnetic field applied to the material, affect the SAR value by changing the hysteresis loop shape and area (*i.e.*, dynamic magnetization response).[3,7,8] Therefore, increasing the saturation magnetization (M_s) and coercive field (H_c) of the nanostructures at the hyperthermia frequency and field strength is predicted to enhance the SAR.

Effective magnetic anisotropy is a measure of a material's resistance to magnetization and is responsible for the shape of the hysteresis loop.[9] It is influenced by factors such as magnetocrystalline anisotropy, shape anisotropy, surface anisotropy, and interparticle interactions.[8] It is possible to enhance the SAR value by the modulation of these factors. For instance, theoretical and experimental studies have demonstrated that

[a] Department of Materials Science and Engineering, Izmir Institute of Technology, 35433 Izmir, Turkey
[b] Italian Institute of Technology, via Morego 30, 16163 Genoa, Italy. E-mail: teresa.pellegrino@iit.it
[c] Chemical and Chemical Industry Department, via Dodecaneso, 31, 16146 Genoa, Italy
[d] Department of Photonics, Izmir Institute of Technology, 35433 Izmir, Turkey

iron oxide nanocubes (IONCs) exhibit a higher SAR than spherical ones, which is attributed to their reduced number of facets and lower level of disordered spin at their surface.[10] Furthermore, in recent experimental studies, SAR values of various morphologies of iron oxide nanocrystals (*i.e.*, nano-flowers, nanooctahedra, nanorods, and nanocubes) have been comprehensively compared and among these, the SAR values of IONCs outperformed all other morphologies since shape anisotropy produces an easy axis of magnetization along the long axis, which is missing in spherical ones.[3]

Another approach to increase the SAR is to form nanoparticle assemblies in a chain-like or columnar structure, enabling dipolar coupling between neighboring nanoparticles.[10–16] Dipolar coupling between magnetic nanocrystals constrains their degree of freedom in motion under an applied magnetic field, leading to increased coercivity, enhanced hysteresis losses, and ultimately greater heat generation.[17,18] Furthermore, the fact that magnetosome particles, magnetic nanocrystals formed naturally by magnetotactic bacteria, linearly assembled in chains in magnetotactic bacteria, showing enhanced heating under alternating magnetic fields (AMFs), together with the observation that magnetic nanoparticles in suspension tend to form linear clusters under a uniform magnetic field, has sparked interest in deliberately engineering such linear structures to boost hyperthermia performance.[19] However, the effect of the tendency to form oriented structures under a magnetic field can be disrupted when the magnetic field is removed unless the particles are fixed in a matrix or template.[20] Moreover, attempting to achieve random chain formation *via* high particle concentration may lead to aggregation, resulting in lower SAR values.[21]

In this context, assembling magnetic nanoparticles on a one-dimensional (1D) anisotropic template is a promising strategy to enhance their heating performance under applied AMFs. Several studies have reported hybrid nanocomposites composed of anisotropic nanostructures and iron oxide nanoparticles.[22–30] However, most of these studies have primarily focused on the magnetic manipulation of the template particles,[22–27] whereas the dynamic magnetic properties and magnetic heat losses of superparamagnetic nanoparticles exhibiting chain-like or columnar-like arrangements on templates have not yet been reported. For instance, zinc oxide nanorods,[31] gold nanorods,[32] silicon nanowires,[28,33] and silver nanowires[34,35] (AgNWs) have been decorated with iron oxide nanoparticles for diverse applications, including biomedical imaging, magnetic resonance technologies, chemo-photothermal synergistic cancer therapy, flexible electronics, and electromagnetic interference shielding. Among these anisotropic structures, AgNWs are attractive due to their notable surface chemistry versatility, which enables straightforward functionalization with biocompatible polymers or targeting ligands. Their high aspect ratio makes them an excellent 1D template for constructing multifunctional nanostructures, especially for biomedical purposes.[28] Also, owing to their high reactivity toward oxidants, AgNWs can also serve as sacrificial templates that are selectively etched to yield silver-free 1D nanostructures.[36–38]

AgNWs have been investigated for cancer therapy owing to their intrinsic anticancer activity and potential as drug delivery platforms.[39–41] Studies have demonstrated that AgNWs can act as potent therapeutic agents by inducing ROS mediated apoptosis and enhancing tumor cell death.[39,41–43] The tumor environment, the particle morphology, and the type of surface coating can significantly influence the release of Ag^+ ions from silver nanoparticles.[42,44–47] Indeed, their biomedical applications remain limited due to silver-related biotoxicity, including nonspecific damage to healthy cells such as fibroblasts and red blood cells, as well as inflammatory responses related to their high aspect ratio.[42,46,48–52] Nevertheless, incorporating AgNWs into a hydrogel or polymer matrix by intratumoral administration may enable localized and controllable therapy with intrinsic antibacterial/cytotoxic antitumoral activity, making them suitable for topical applications such as in skin melanoma.[48,53,54]

Although several studies have investigated the decoration of AgNWs with iron oxide nanoparticles, they have not focused on tailoring these hybrid structures for magnetic hyperthermia applications and determining the effect of long-range ordered iron oxide nanoparticle clusters on their dynamic magnetic properties and SAR performances.[22,34,35,55–58]

Here, a new approach is presented that enables the formation of chain-like structures to improve the SAR values of IONCs. The high aspect ratio and surface area of AgNWs were used as a template to obtain chain-like assemblies of IONCs. Thus, the magnetic anisotropy of IONCs, known for their high heating efficiency due to their shape anisotropy, was further enhanced by assembling them in a 1D structure to increase the SAR values. For this, IONCs were synthesized using the solvothermal method since this method has been proven to scale production at the gram-scale while maintaining high-quality iron oxide nanoparticles with benchmark magnetic heat losses.[59] Their surfaces were functionalized with poly-ethyleneimine (PEI) by post-synthesis and attached to the AgNW surface *via* electrostatic forces. The heating efficiency of the nanostructures was investigated by alternating current (AC) magnetometry at various frequencies (*i.e.*, 110, 200, and 300 kHz) and magnetic field strengths (*i.e.*, 12, 16, and 24 kA m^{-1}), revealing better magnetic heating performance than the corresponding individual IONCs at the same dose.

Experimental section

Materials

Iron(0) pentacarbonyl (>99.99% trace metal bases), 1-octanol (anhydrous, ≥99%), oleic acid (≥99%, G.C.), benzaldehyde (≥99%, ReagentPlus), hexadecylamine (98%), ethyl acetate (ACS reagent, ≥99.5%) acetonitrile (≥99.9%), sodium (*meta*) periodate (≥99.0%), glycerol (ACS reagent, ≥99.5%), silver nitrate (AgNO₃, ACS reagent, ≥99.5%), iron(III) chloride hexahydrate (FeCl₃·6H₂O, ACS reagent, 97%), polyvinylpyrrolidone

(PVP, average M_w~1 300 000 and M_w~40 000), nitric acid (65%, for trace analysis), chloroform, acetone, toluene, and ethanol (ACS reagent, ≥99.5%) were purchased from Sigma-Aldrich. Polyethyleneimine (branched, M_w. 10 000, 99%, Alfa Aesar) was purchased from Thermo Fisher Scientific. All chemicals were used as received without further purification. Milli-Q water with an electrical resistivity of 18.2 MΩ cm was used for all experiments.

Synthesis of AgNWs

The synthesis of AgNWs was conducted as described by Sarisozen *et al.*[60] In the synthesis, 5.0 mL of glycerol was transferred to a 40 mL glass vial and heated to 160 °C while stirring magnetically at 200 rpm for 2 h. Then, 4.0 mM $FeCl_3 \cdot 6H_2O$ was dissolved in water, and 0.160 mL of the solution was added to this vial. After that, 2.5 mL of 0.1 M $AgNO_3$ and 2.5 mL of 0.6 M PVP (M_w~1 300 000), each dissolved in glycerol–water solvent mixtures (with volume ratios of 4 : 1 and 2 : 3, with respect to iron, respectively), were mixed in a 15 mL conical centrifuge tube and then added dropwise to the hot glycerol solution. Subsequently, the magnetic stirring bar was removed, and the reaction solution was left at 160 °C for another 2 h. The reaction was stopped by placing the glass vial into an ice-water bath. The synthesized AgNWs were purified to remove irregularly shaped nanoparticles and other reaction by-products using an anti-solvent precipitation method with acetone. The AgNW solution was diluted with water, and acetone was added dropwise until precipitation occurred. The supernatant was carefully removed, and the precipitated nano-wires were redispersed in a 0.5% w/v aqueous solution of PVP (M_w ~ 40 000). This step was repeated four times. Finally, the purified AgNWs were dispersed in 4 mL of isopropyl alcohol and centrifuged (2000 rpm, 20 min) to remove excess PVP. After centrifugation at 376 rcf for 20 min (Centrifuge 5424, Eppendorf), the supernatant was discarded, and the AgNWs were dispersed in water. The washing step was repeated four times. After the final washing, the AgNWs were dispersed in 4 mL of water for subsequent use.

Synthesis of IONCs

15 ± 1 nm IONCs were synthesized *via* the solvothermal method, as reported in the work of Gavilán *et al.*[61] Briefly, a homogeneous solution of 1-octanol (7.5 mL), hexadecylamine (0.2 g), and oleic acid (0.6 mL) was prepared in a glass vial using a magnetic stirrer at 800 rpm and 60 °C for 30 min. After that, the solution was cooled to room temperature (RT), and then iron pentacarbonyl (1.5 mL, 11.1 mmol) and benz-aldehyde (1.0 mL, 9.8 mmol) were added and stirred at 800 rpm and RT for 20 min. Then, the prepared solution was transferred to a 25.0 mL Teflon vessel inserted in an autoclave reactor. The autoclave reactor was placed in an oven at 200 °C and left for 4 h. At the end of the reaction time, the autoclave was removed from the oven and allowed to cool to ambient temperature. Then, the sample solution was split into two Falcon tubes of 50 mL, adding 30 mL each of acetone as an antisolvent to precipitate the nanoparticles. Finally, nano-particles were recollected upon centrifugation (4500 rpm, 20 minutes) and redispersed in 20 mL of $CHCl_3$.

Surface functionalization of IONCs

For the surface functionalization of IONCs with a PEI polymer, we adapted an already published protocol with some modifications.[62,63] In the experimental procedure, 0.5 mL of IONCs (3.18 mg_{Fe} mL^{-1}) in $CHCl_3$ was transferred to a 2 mL centrifuge tube, and 1.5 mL of acetone was added. This solution was vortexed for 10 s and centrifuged at 1500 rpm for 5 min. The supernatant of the solution was discarded, and IONC precipitates were dried with N_2 and redispersed in 0.5 mL of toluene. Then, 0.1 mL of ethyl acetate and 0.1 mL of acetonitrile were mixed in a round-bottom glass flask, and 0.125 mL of IONC solution in toluene was added to this mixture. After that, 0.28 M sodium periodate solution was prepared in water, and 0.15 mL of it was added to the solution as an oxidizing agent. The solution was sonicated in an ultra-sonic bath for 20 min by keeping the temperature between 30 and 35 °C at 45 kHz. At the end of sonication, IONCs were separated magnetically, and the supernatant was discarded. The precipitate was washed with ethanol twice and distilled water three times to remove excessive reactants by magnetic separation. At the end of this step, the hydrophilic IONCs functionalized with the –COOH group were obtained and called IONCs@COOH. To perform the adsorption of PEI on the IONCs@COOH surface, first, PEI is dissolved in water at a concentration of 20 mg mL^{-1}. Then, 6 mL of this PEI solution was placed in a vial and sonicated while IONCs@COOH solution (0.30 mL, 3.33 mg_{Fe} mL^{-1}) was added dropwise. This solution was sonicated for a further 3 h in the ultrasonic bath. After that, the solution was washed five times with water by membrane-filtered centrifuge tubes (Millipore Sigma, Amicon membrane filters of 100 kDa MWCO), redispersed in water, and sonicated with a probe sonicator at 45 kHz for 10 min. These samples were referred to as IONCs@PEI.

Assembly of IONCs on AgNWs

For the decoration of IONCs@PEI on AgNWs, 5.0 mL of concentrated IONCs@PEI solution (1.08 mg_{Fe} mL^{-1}) was prepared in a glass vial and placed in a vortex shaker (multi-reax vortex shaker, Heidolph). Then, 0.5 mL of AgNW colloidal solution (0.96 mg_{Ag} mL^{-1}) was added all at once to the IONCs@PEI solution while placed in a vortex shaker at 400 rpm and left for several hours. The IONCs@PEI attached to AgNW samples was referred to as AgNWs@IONCs@PEI. After that, to remove non-attached IONCs@PEI nanoparticles, the mixture was centrifuged at 2000 rpm for 30 min. This step was repeated two times, and the final precipitates of AgNWs@IONCs@PEI were dispersed in water.

Ag$^+$ ion release experiment

To evaluate the potential release of Ag$^+$ ions under physiologically relevant conditions, 250 μL of the Ag nanowire suspension (0.25 mg mL^{-1}) was mixed with 750 μL of phosphate-buffered saline (PBS, pH 6.5, without NaCl) and incubated for

different time points (3 h, 24 h, and 72 h). Following incubation, the suspensions were centrifuged at 2000 rpm for 10 minutes to separate the wires from the supernatant. The concentration of the etched Ag^+ ions in the supernatant was subsequently quantified by elemental Ag analysis using ICP-OES.

Characterization

A scanning electron microscopy (SEM) image of the AgNW sample was captured using a JEOL JSM-6490LA instrument at an acceleration voltage of 10 kV with a secondary electron detector. Transmission electron microscopy (TEM) was employed to observe the size, morphology, and assembled structures of IONCs@PEI on AgNWs and of the initial building blocks, using a JEOL JEM-1400 microscope operating at 120 kV. For TEM sample preparation, diluted nanoparticle solutions were dropped onto 200-mesh carbon-coated copper grids. The particle size and size distribution of AgNW and IONC samples were determined from electron microscopy images using ImageJ software.

The hydrodynamic size (d_h), size distribution, and surface zeta potential measurement of the nanoparticles were measured using dynamic light scattering (DLS) with a Zetasizer (Nano ZS90, Malvern, UK). Each DLS measurement was performed in triplicate. The pH of the reaction medium was determined using pH indicator paper strips. Ultraviolet-visible (UV-Vis) spectroscopy was used to confirm the successful synthesis of AgNWs. The surface chemistry of the nanoparticles was analyzed by Fourier transform infrared spectroscopy with an attenuated total reflectance configuration (ATR-FTIR) using a Vertex 70 V Bruker instrument. Raman spectroscopy was performed to examine the phases of the IONCs. The samples were dried on aluminum foil and analyzed using a Renishaw inVia Reflex confocal Raman microscope. A 50× objective lens was used to focus the laser beam with an excitation wavelength of 785 nm onto the dried samples, and analysis was performed with 1% laser power (2.87 mW), 10 s exposure time, and five accumulations. The X-ray diffraction (XRD) pattern of the nanoparticles was obtained using a PANalytical Empyrean X-ray diffractometer equipped with a 1.8 kW Cu Kα ceramic X-ray tube and a PIXcel3D 2 × 2 area detector, operating at 45 kV and 40 mA. For XRD analysis, concentrated nanoparticle solutions were dropped onto a zero-diffraction quartz wafer. Elemental analysis was performed using inductively coupled plasma optical emission spectroscopy (ICP-OES, Thermo Fisher CAP 6000 series). For ICP-OES preparation, 0.01 mL of nanoparticle solution was mixed with 1.0 mL of nitric acid and left overnight for digestion. The solution was then diluted to 10.0 mL with Milli-Q water and filtered through a 0.45 μm PTFE membrane. The dynamic magnetization curves of the hydrophilic magnetic nanoparticles, Ag NWs, and AgNWs@IONCs@PEI were measured using an AC magnetometer (AC Hyster Advance, Nanotech Solutions) at frequencies of 110, 200, and 300 kHz, with applied magnetic fields of 12, 16, and 24 kA m^{-1} at 20 °C. Each set of AC magnetometer measurements was repeated

three times for consistency. The instrument automatically calculated SAR values based on the magnetic hysteresis loops obtained during the AC field cycling using the equation given below, where A is the area of the hysteresis loop, f is the frequency of the alternating magnetic field, and c is the Fe concentration in the sample.

$$\text{SAR} = \frac{Af}{c}$$

To study the stability of the assembly, calorimetric measurements were conducted at a frequency of 182 kHz and a field amplitude of 39 kA m^{-1} (DM100 Series, nanoScale Biomagnetics Zaragoza, Spain) with the sample (100 μL at 0.125 g L^{-1} of Ag and 0.05 g L^{-1} of Fe) exposed for three cycles of 30 min each to AMF and the temperature profiles recorded using a fiber-optic temperature probe. Aliquots of the sample are taken every 30 min of the AMF cycle to prepare TEM grids.

Statistical analysis

Statistical analyses on SAR and H_c values were performed using one-way ANOVA followed by Tukey's *post-hoc* test to determine significant differences between sample groups using OriginPro 9 software. Results were considered statistically significant when $p < 0.05$. Groups that did not differ significantly shared the same letter label (a, b, or c) in the Tukey grouping table.

Results and discussion

A new nanocomposite structure was designed to enhance the SAR and improve the heating efficiency of IONCs under an alternating magnetic field. Thus, IONCs were assembled onto the surface of AgNWs in a chain-like or columnar arrangement. For this purpose, AgNWs and IONCs@PEI were synthesized separately, and the IONCs@PEI was subsequently attached to the AgNWs *via* non-covalent interactions by introducing the AgNWs into an aqueous dispersion of concentrated IONCs@PEI.

AgNWs were synthesized by the previously reported polyol method.[60] This method is based on the reduction, nucleation, and subsequent one-dimensional growth of silver precursor (AgNO$_3$) into nanowires, facilitated by a polyol solvent (glycerol, serving also as a reducing agent), a stabilizer (PVP), and a transition metal salt-based promoter (FeCl$_3$·6H$_2$O). FeCl$_3$·6H$_2$O scavenges atomic oxygen from silver nanocrystallite surfaces, provides electrostatic stabilization, and promotes AgCl formation. Since AgCl is less soluble than AgNO$_3$, Ag$^+$ is released slowly, reducing the reaction rate and favoring anisotropic growth.[64] SEM images of the AgNWs and the corresponding length size distribution graph are presented in Fig. S1a and S1b, respectively. The length and diameter of the AgNW samples were measured using ImageJ software and were found to be 9 ± 7 μm and 109 ± 27 nm, respectively. The UV-Vis spectrum of the synthesized AgNWs is shown in Fig. S1c. The characteristic absorption peaks of the AgNWs

formed were observed at approximately 350 and 380 nm, corresponding to the excitation of transverse plasmon resonances.[65] For AgNWs of this length, the longitudinal plasmon resonance is present beyond 800 nm. Beyond 380 nm, the spectrum is dominated by the combined effects of scattering and extinction rather than a distinct plasmon resonance.[66,67]

The IONCs with a well-defined cubic morphology were synthesized using the solvothermal method.[61] TEM images and particle size distributions of IONCs are shown in Fig. 1b and e, respectively. The mean particle size of IONCs was determined to be 15 ± 1 nm with a homogeneous size distribution (Fig. 1b and Fig. S2).

The surface of the as-synthesized IONCs is hydrophobic due to the oleic acid molecules on their surfaces. To make

them water-soluble while maintaining colloidal stability, the surface of IONCs was functionalized with PEI and only then attached onto the surface of AgNWs. The PEI coating procedure was modified from those in previously reported studies.[62,63,68] In this procedure, first, oleic acid is oxidatively cleaved into pelargonic acid and azelaic acid in the presence of sodium periodate, acetonitrile, and ethyl acetate, and the azelaic acid molecules remain on the surface of IONCs, yielding hydrophilic IONCs functionalized with carboxylic acid groups (IONCs@COOH). The presence of carboxylic acid groups on the IONC surfaces, which confers negative charges to the IONC surface, enables the adsorption of positive PEI polymer molecules. To notice that while the first step of oxidation of oleic acid by periodate was followed as reported in
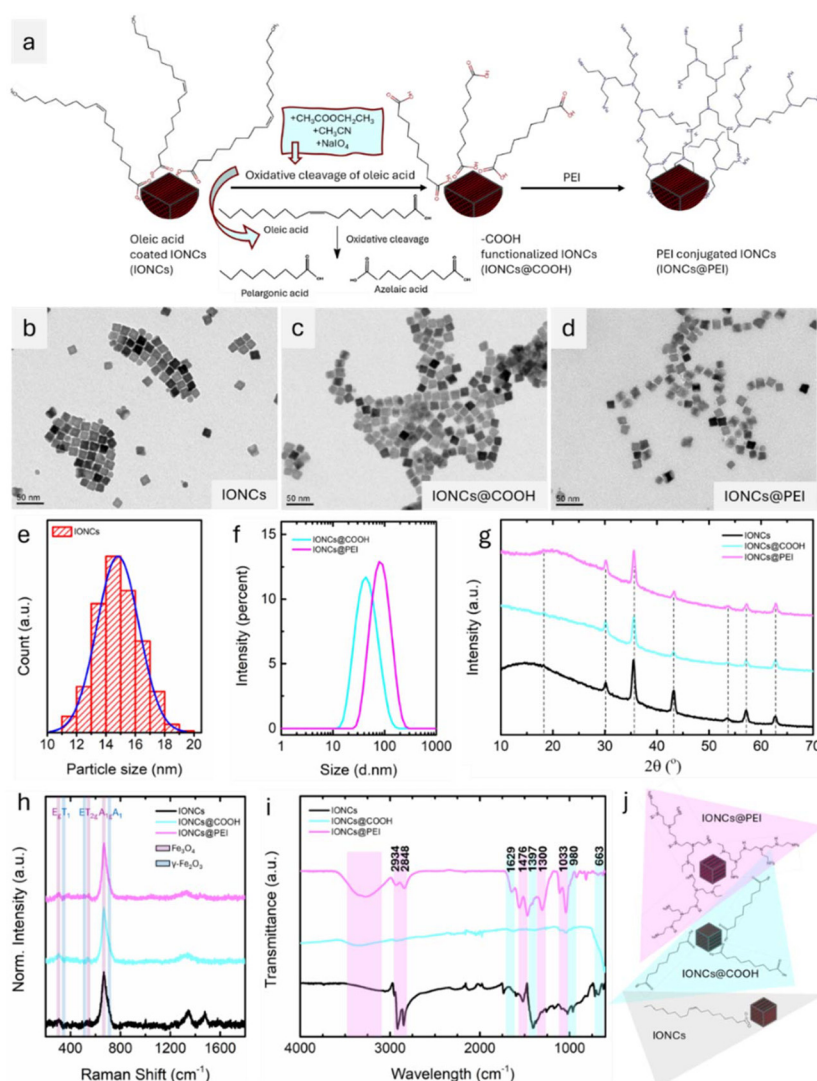
Fig. 1 Morphology, size distribution, and structural features of IONCs, IONCs@COOH, and IONCs@PEI. The scheme of the applied surface modification procedure to IONCs (a). The TEM images of IONCs (b), IONCs@COOH (c), and IONCs@PEI (d). The particle size distribution of IONCs measured by statistical analysis on more than 200 objects selected from different TEM images (e) and the hydrodynamic particle size distribution graphs of IONCs@COOH and IONCs@PEI samples by intensity (f). The XRD pattern (g), Raman (h), and ATR-FTIR spectrum (i) of IONCs, IONCs@COOH, and IONCs@PEI. The schematic of the surface functional groups of IONCs, IONCs@COOH, and IONCs@PEI (j).

the original reference work,[62] at the second stage, we do adsorb the positive PEI polymer on the negative charge nanocubes[63] rather than covalently link the amine group of PEI to the carboxylic groups of azelaic acid at the spherical nanoparticle surface by EDC chemistry as originally reported. The representative surface modification mechanism and the experimental procedure for the PEI coating of IONC surfaces are given in Fig. 1a and Scheme S1 of the SI. To highlight that in this study, the ratios of ethyl acetate, acetonitrile, and $NaIO_4$ used for the oxidation were kept constant, while the amount of Fe_3O_4 added to the solution was increased. As a result, the $NaIO_4/Fe_3O_4$ molar ratio was reduced to 1/6 of that used in the reference study from which the procedure was adapted.[62] Additionally, the PEI conjugation step, performed in an ultrasonic bath following oxidation to enable electrostatic adsorption of PEI onto the nanocubes was conducted for 3 h.[63]

The obtained particles were thoroughly characterized at each stage of the surface modification process. As shown in Fig. 1c and d, TEM analysis of water-dispersed solutions confirmed the presence of agglomeration-free particles for IONCs@COOH and IONCs@PEI samples, respectively (only a single carpet of individually coated nanoparticles is visible). The aqueous hydrodynamic size and zeta potential of the IONCs@COOH and IONCs@PEI samples were obtained by dispersing the nanoparticles in deionized water under neutral conditions and analyzing them using DLS. Hydrodynamic size (H_d) versus intensity graph demonstrated unimodal particle size distributions of both IONCs@COOH and IONCs@PEI samples (Fig. 1f). The H_d values were found to be 49 ± 23 nm and 90 ± 38 nm by intensity with PDI values of 0.197 and 0.186 for IONCs@COOH and IONCs@PEI samples, respectively. The standard deviations ($\pm$) indicate the breadth of the size distribution around each mean value. PEI formed a thicker hydration layer around the IONCs due to its bulky, highly branched structure and a high density of protonated amine groups, which is visible on the TEM grid in between nanoparticle spaces compared to small dicarboxylic azelaic acid, which instead is not really visible and will engage in

extensive hydrogen bonding and electrostatic interactions with the AgNWs in water.[69,70] The zeta potential distributions were found to be -15.4 ± 11.4 mV for IONCs@COOH and $+36.1 \pm 12.4$ mV for IONCs@PEI, which confirmed the successful modification and coating of the surface of IONCs with a positively charged PEI polymer (Fig. 2).

The XRD pattern, Raman, and ATR-FTIR spectrum of the IONC, IONCs@COOH, and IONCs@PEI samples are given in Fig. 1g, h, and i. The XRD patterns, as expected, showed that all samples had the same diffraction peaks, which are well-matched with the magnetite phase of iron oxide (Fe_3O_4) with the ICDD card number 75-0033, indicating that the crystal phase of the particles was preserved during the surface functionalization steps. Raman spectroscopy was used to investigate the magnetic phases and possible oxidation of IONCs during their transfer into water and subsequent surface coating with PEI. The acquired Raman spectra also revealed that all IONCs, regardless of their surface ligands (i.e., (oleic acid)IONCs, IONCs@COOH, and IONCs@PEI), have a dominant magnetite phase (Fe_3O_4) with a prominent Raman shift at 670 cm^{-1}, along with smaller bands at 310 cm^{-1} and 540 cm^{-1}.[71] These findings confirmed the preservation of the magnetite phase throughout the transfer and coating processes. In contrast, oxidation to the maghemite phase (γ-Fe_2O_3) after the oxidative cleavage of oleic acid by sodium (meta)periodate was negligible, as no significant maghemite peaks were observed in the Raman spectra at 350 cm^{-1}, 512 cm^{-1}, or 720 cm^{-1} in any of the samples. Additionally, for the IONC sample, the bands at around 1300 and 1450 cm^{-1} confirmed the presence of oleic acid on the surface as the main surfactant.[72] The disappearance of these bands in the other samples indicated a successful change in the polymer surface provided by the conversion of oleic acid into azelaic acid at the first stage and the presence of PEI at the second stage. The schematic representations of functional groups on the surface of the IONCs are shown in Fig. 1j. The functional groups present on the surface of the samples were identified using ATR-FTIR spectroscopy. In the ATR-FTIR spectrum of
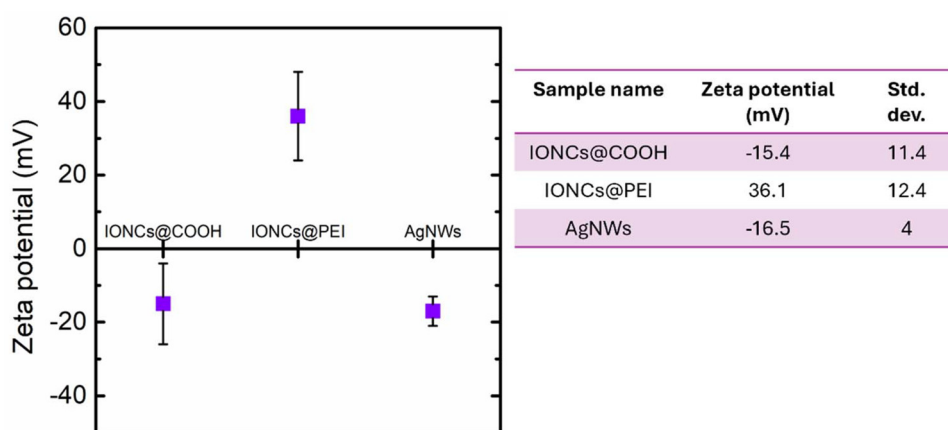

Sample name	Zeta potential (mV)	Std. dev.
IONCs@COOH	-15.4	11.4
IONCs@PEI	36.1	12.4
AgNWs	-16.5	4

Fig. 2 Zeta potential graph and values of IONCs@COOH, IONCs@PEI, and AgNWs.

IONCs, the strong bands at 2930 and 2850 cm^{-1} correspond to the alkyl chains of oleic acid, which are observed as asymmetric and symmetric C–H stretching vibrations, respectively.[73] The weak peak at around 3005 cm^{-1} is attributed to the unsaturated (cis) C–H stretching of oleic acid, and a sharp peak at around 1410 cm^{-1} corresponds to the –C–O–H in-plane bending.[74] For IONCs@COOH, the peaks at 1629 and 1397 cm^{-1} could be assigned to the stretching vibration of C=O and bending vibrations of CH$_2$, respectively, of the azelaic acid. It is observed that, following the oxidative cleavage of oleic acid, the intensities of the bands near 2930 and 2850 cm^{-1} are significantly reduced for the IONCs@COOH, indicating a decreased amount of CH$_2$ and CH$_3$ groups. The broadband observed in the spectrum of IONCs@PEI between 3400 and 3200 cm^{-1} was attributed to the N–H stretching vibrations of primary and secondary amines. The 2934 and 2848 cm^{-1} peaks were associated with the C–H stretching vibrations of methylene groups. The weak to medium peaks observed between 1600 and 1500 cm^{-1} were assigned to the N–H bending vibrations. Three absorption peaks at 1476, 1300, and 1033 cm^{-1} could be attributed to the C–N stretching vibrations.[75] The appearance of N–H bending and C–N and stretching vibrations in the IONCs@PEI FTIR spectrum confirms the successful surface functionalization of the IONCs with PEI.

The zeta potentials of IONCs@COOH, IONCs@PEI, and AgNWs were measured in deionized water at a pH range of 6–7 (determined using pH indicator paper strips) and a temperature of 20 °C (Fig. 2). The surfaces of IONCs@PEI were positively charged, while the surfaces of AgNWs were negatively charged due to the presence of PEI and PVP polymers, respectively. Fig. 3a presents a schematic representation of the experimental procedure for assembling IONCs on AgNWs. TEM images of AgNWs and AgNWs@IONCs@PEI particles at various magnifications are shown in Fig. S3a–c and Fig. S3d–f, respectively. Neither the entanglement of AgNW nor the agglomeration of IONCs@PEI was observed. The distribution of IONCs@PEI on the PVP-stabilized AgNW surface was primarily homogeneous but not in a perfect chain-like structure. Fig. 3e reveals that IONCs@PEI assembled into long-range ordered clusters along AgNWs, spanning lengths above 1 μm. Provided that each IONCs has a cube edge of ~15 nm, the observed ordering ideally would extend over distances of more than 67 times the particle size, indicating strong directional assembly, which is not reported in previous studies.[22–30] Under neutral conditions, PEI-coated nanoparticles exhibit positively charged surfaces due to the protonation of their amine groups.[76] PVP stabilizes Ag$^+$ ions through coordination with carbonyl groups, leaving partially negative oxygen atoms on the AgNW surfaces.[77] The electrostatic attraction between the positively charged IONCs@PEI and the negatively charged PVP stabilized AgNWs drives their aggregation and interfacial bonding.[78] Consequently, the oriented clustering of IONCs@PEI nanoparticles onto AgNWs was primarily due to the opposite surface zeta potentials, accompanied by van der Waals forces.[24,79]
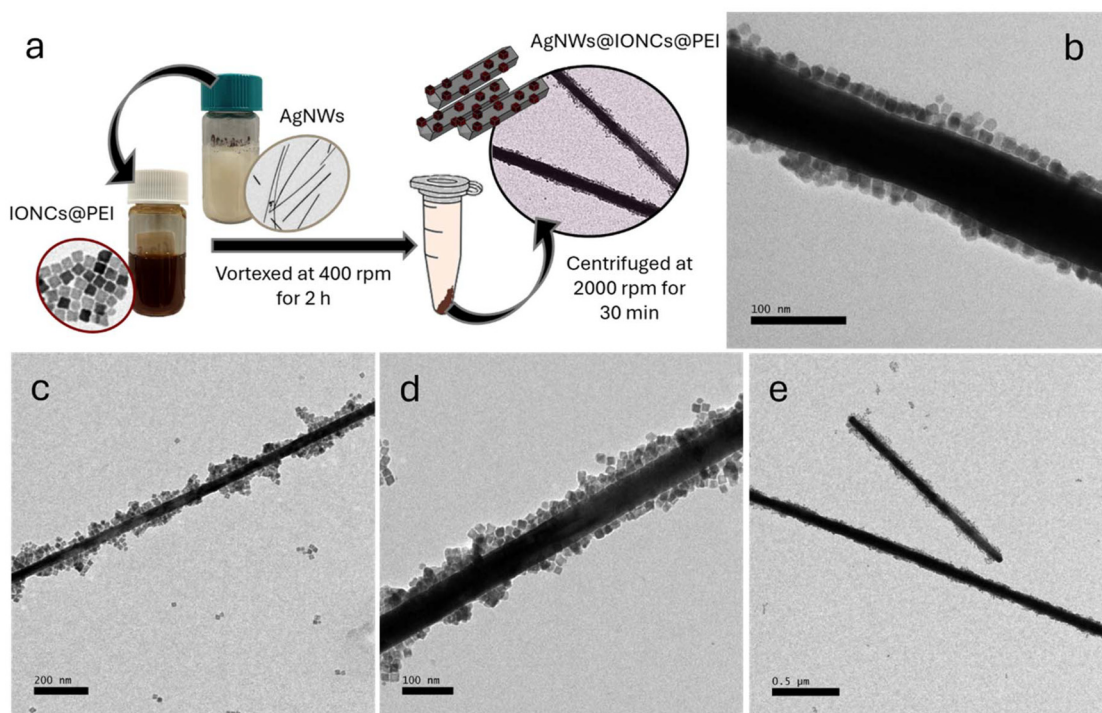
Fig. 3 Schematic illustration of the experimental procedure for IONC assembly on AgNWs (a). TEM images of AgNWs@IONCs@PEI at various magnifications (b–e).

To note that in the attempt to optimize the assembly protocol, initial studies were conducted with IONCs modified with polydopamine (PD) having a surface charge of around -11.4 ± 4.7 mV in water as determined by zeta potential measurements. Details of the surface functionalization procedure are given in the SI. When mixing these PD-coated IONCs (IONCs@PD) with AgNWs, although IONCs@PD decorated the AgNW surface, large clumps of IONCs@PD were present on the AgNWs (Fig. S4a and S4b). It is worth mentioning that already IONCs@DP was forming some small clusters even before mixing them with the AgNWs (Fig. S4c–e) and this has likely affected the assembly formation. Therefore, to avoid surface aggregation and better control the assembly formation, the choice of PEI and the use of positively charged IONCs were critical for obtaining homogeneously distributed IONCs on the AgNWs.

The change in interfacial stability between IONCs@PEI and AgNWs in a neutral aqueous medium is shown in Fig. S5. TEM images of AgNWs@IONCs@PEI on the day of synthesis show that IONCs@PEI are uniformly bound to the AgNW surfaces, with a clear, distinct interface and some of the IONCs@PEI are not bound. The same type of TEM images with not much significant differences are recorded one and three days later, suggesting the stability of the assembly in a short period and in a neutral aqueous environment.

The colloidal stability of AgNWs@IONCs@PEI assemblies was evaluated by dispersing them in water. Photographs of the dispersions were taken over time to monitor their stability (Fig. S6). The assemblies in water began to sediment at the bottom of the vials within a few hours, and complete precipitation was observed after three days, providing their relatively micrometer size, which promotes sedimentation through gravitational effects. However, even after three days, upon shaking the vial, the solution turned back to the original brownish color and appeared as the one at day one. Furthermore, Fig. S7 shows the good dispersion of AgNWs@IONCs@PEI in water and their response to a permanent magnet, confirming that the nanowires are uniformly coated with IONCs and can be efficiently separated using a standard lab magnet (0.3 T). The stability of AgNWs@IONCs@PEI was also evaluated by dispersing them in common biological media such as phosphate-buffered saline (PBS, pH 6.5) and complete DMEM (containing 10% FBS, used DMEM phenol red free to facilitate visualization). Photographs of the dispersions were taken within the first 24 h to monitor their stability in PBS and in DMEM (Fig. S8). While the composites were initially well-dispersed in PBS and complete DMEM, AgNWs@IONCs@PEI exhibited faster sedimentation and aggregation, particularly in DMEM, likely due to the serum protein content. TEM images of AgNws@IONCs@PEI after 24 h in PBS (Fig. S8b) showed that the composites largely retained their morphology and maintained the interactions between AgNWs and IONCs@PEI. Instead, composites incubated in DMEM showed less integrity and detached IONCs from AgNWs (Fig. S8d).

To evaluate the Ag$^+$ ion release and thereby the possible toxicity of our structures, we incubated AgNWs in PBS (at pH 6.5 to mimic the acidic tumor pH) for several hours (3 h, 24 h, and 72 h) and analyzed the supernatant by means of released Ag ions by ICP-OES. The measured Ag$^+$ concentrations were below the instrument's detection limit (<0.01 mg L^{-1}) for the sample incubated for 3 h, indicating negligible ionic silver release under these conditions. However, we found 0.01 g L^{-1} and 0.0375 g L^{-1} of Ag release after the incubation of AgNWs in PBS for 24 h and 72 h of incubation, respectively. This observation agrees with previous reports showing that AgNWs exhibit minimal but still present Ag$^+$ release.[80,81] However, the release of Ag$^+$ ions, also associated with the generation of ROS, is strongly influenced by the particle dose, morphology, and surface coatings.[82] By carefully controlling these parameters, the intrinsic toxicity of silver nanowires can be effectively regulated and controlled to facilitate topical release, for instance, to a tumor site.

The dynamic hysteresis loops of the hydrophilic magnetic nanoparticles were evaluated using AC magnetometry at various frequencies and under various magnetic fields. The magnetic properties of the nanoparticles can be determined from the hysteresis loop, such as coercive field (H_c), saturation magnetization (M_s), and remanence (M_r). These data provide information about magnetic interactions and possible arrangements of nanoparticles.[83,84]

The applied field conditions stretched beyond the clinically suitable value ($H_{AC}f \leq 5 \times 10^9$ A m^{-1} s^{-1}) of magnetic hyperthermia therapy as part of this proof-of-concept study. In this study, only one of the AC magnetization conditions, 24 kA m^{-1} at 300 kHz (7.2×10^9 A m^{-1} s^{-1}), lies outside the clinical safety limit.[3] Furthermore, the present work is a proof-of-concept study demonstrating the material's development at this stage. The iron concentration of the IONCs@COOH and IONCs@PEI samples used in the AC magnetometer measurement was 0.6 mg$_{Fe}$ mL^{-1}, while the iron concentration of the AgNWs@IONCs@PEI sample was 0.15 mg$_{Fe}$ mL^{-1}.

The magnetization curves of the IONCs@COOH, IONCs@PEI, and AgNWs@IONCs@PEI samples are given in Fig. 4. For all samples, a non-saturated hysteresis loop was observed at 12 and 16 kA m^{-1} magnetic fields, independent of the frequency of the field being applied. However, hysteresis loops reached saturation when the magnetic field strength was increased to 24 kA m^{-1}. It has been reported that a higher H_{AC} field is required to achieve saturation magnetization.[84] It was also observed that PEI conjugation on the IONCs@COOH surface slightly reduced the magnetization curve area by 3–25%, except under the conditions of 24 kA m^{-1} and 110 kHz (Table S1). This reduction can be attributed to the increased hydrodynamic size of the IONCs@PEI sample, which influences the nanoparticle relaxation behavior.[85] When comparing the hysteresis loop responses of IONCs@PEI and AgNW@IONCs@PEI samples at varying H_{AC} amplitudes and frequencies, the loop area of AgNW@IONCs@PEI was 12–28% smaller than that of IONCs@PEI at 12 kA m^{-1}. As the H_{AC} amplitude increased to 16 kA m^{-1}, the reduction in the AgNW@IONCs@PEI loop area decreased to 5–10%. At 24 kA m^{-1}, the AgNW@IONCs@PEI sample exhibited the largest hys-
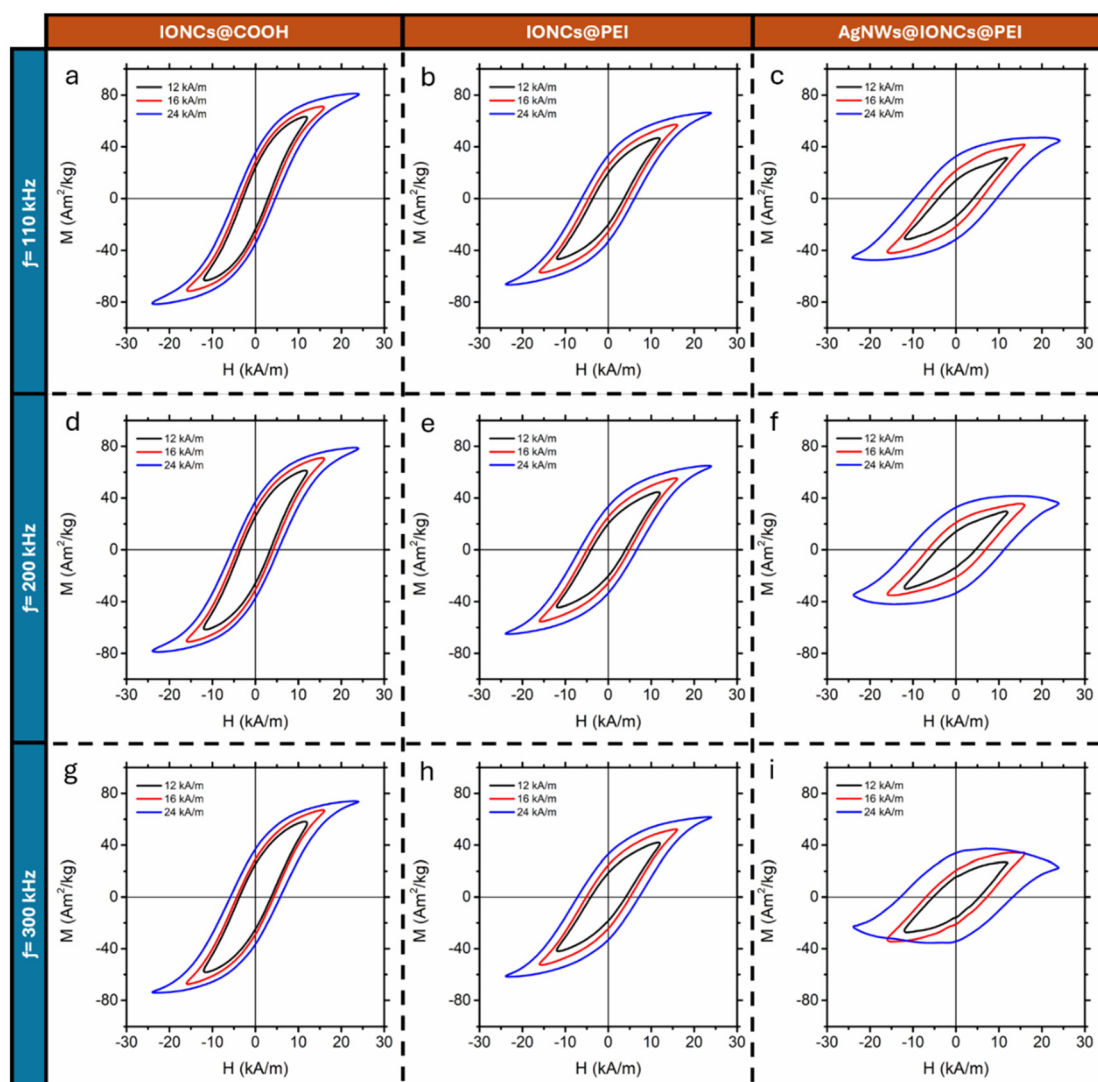
Fig. 4 AC hysteresis loops of IONCs@COOH (a, d and g), IONCs@PEI (b, e and h), and AgNWs@IONCs@PEI (c, f and i) at various frequencies and magnetic field strengths.

teresis loop area among all samples, increasing by 16% at 110 kHz and by 18% at both 200 and 300 kHz relative to IONCs@PEI.

To determine whether AgNWs influence the dynamic hysteresis loops of AgNW@IONCs@PEI, AC magnetometry measurements of AgNWs alone were performed under the same frequency and magnetic field strength conditions, as presented in Fig. S9. At frequencies of 110 and 200 kHz, the AgNWs exhibited negligible diamagnetic contribution to the synthesized nanocomposite structure. However, under the conditions of 300 kHz and 24 kA m^{-1}, a noticeable diamagnetic contribution may occur in the AgNWs@IONCs@PEI sample, as shown in Fig. 4i.

To understand the reason for the increase in magnetic loss observed with increasing magnetic field in the AgNW@IONCs@PEI sample, the H_c, M_s, M_r, and M_r/M_s values extracted from the hysteresis loop were evaluated (Table 1). For

all samples, the M_s value decreases with increasing field frequency; this could be attributed to the delay in the magnetization response to the applied AC field.[86] The M_s value of the IONCs@PEI nanoparticles was 26% to 40% higher than that of AgNWs@IONCs@PEI for all examined magnetic field parameters. The imperfectly aligned chain-like structures could cause this behavior. The magnetic moments of the neighboring nanoparticles can be aligned antiparallel, resulting in a decrease in the net magnetization of the system.[3] In addition, the magnetic anisotropy in these structures can create a preferred magnetization direction and limit the ability of nanoparticles to align their magnetic moments in the direction of the applied magnetic field, resulting in a lower saturation magnetization. However, as the applied magnetic field increased, a significant rise in the H_c values of the AgNWs@IONCs@PEI sample was observed. The increase corresponded to 14% and 28% at 110 kHz, 13% and 39% at 200 kHz, and 32% and 39%

Table 1 Dynamic magnetic properties of IONCs@COOH, IONCs@PEI, and AgNWs@IONCs@PEI

| Sample name	H_{app} (kA m^{-1})	H_c (kA m^{-1})	M_s (A m^2 kg^{-1})	M_r (A m^2 kg^{-1})	M_r/M_s	Area (mJ kg^{-1})	SAR (W g^{-1}$_{Fe}$)
110 kHz							
IONCs@COOH	12	2.9 ± 0.0	63.3 ± 0.1	23.8 ± 0.2	0.38	811 ± 6	89 ± 1
	16	3.6 ± 0.0	71.3 ± 0.4	28.3 ± 0.3	0.40	1145 ± 14	126 ± 2
	24	4.7 ± 0.1	81.4 ± 0.5	35.0 ± 0.3	0.43	1804 ± 40	198 ± 4
IONCs@PEI	12	3.6 ± 0.0	46.8 ± 0.3	20.0 ± 0.2	0.43	698 ± 8	77 ± 1
	16	4.6 ± 0.0	57.2 ± 0.3	25.6 ± 0.2	0.45	1099 ± 7	121 ± 1
	24	6.2 ± 0.0	66.6 ± 1.1	33.3 ± 0.1	0.50	1815 ± 22	199 ± 2
AgNWs@IONCs@PEI	12	4.1 ± 0.4	31.6 ± 2.0	13.9 ± 0.7	0.44	503 ± 49	55 ± 5
	16	5.9 ± 0.2	42.3 ± 2.2	21.7 ± 0.7	0.51	1019 ± 67	111 ± 7
	24	9.5 ± 0.2	47.6 ± 1.6	32.1 ± 1.7	0.67	2103 ± 113	231 ± 12
200 kHz							
IONCs@COOH	12	3.5 ± 0.0	61.4 ± 0.1	25.7 ± 0.1	0.42	900 ± 8	179 ± 2
	16	4.2 ± 0.0	71.0 ± 0.6	30.8 ± 0.3	0.43	1286 ± 13	256 ± 3
	24	5.4 ± 0.0	78.9 ± 1.1	37.1 ± 0.5	0.47	1962 ± 51	391 ± 10
IONCs@PEI	12	4.0 ± 0.1	44.5 ± 0.2	20.1 ± 0.5	0.45	720 ± 21	143 ± 4
	16	4.9 ± 0.0	55.4 ± 0.4	25.4 ± 0.1	0.46	1114 ± 1	222 ± 0
	24	6.7 ± 0.0	65.1 ± 0.8	33.4 ± 0.3	0.51	1889 ± 32	377 ± 6
AgNWs@IONCs@PEI	12	4.5 ± 0.4	30.0 ± 1.3	13.7 ± 2.0	0.46	516 ± 87	103 ± 17
	16	6.8 ± 0.1	35.5 ± 1.3	21.1 ± 0.4	0.59	1006 ± 30	200 ± 6
	24	11.2 ± 0.1	41.8 ± 2.0	33.0 ± 0.4	0.79	2229 ± 58	444 ± 12
300 kHz							
IONCs@COOH	12	3.7 ± 0.0	58.2 ± 0.5	25.1 ± 0.1	0.43	901 ± 9	271 ± 3
	16	4.3 ± 0.0	67.3 ± 0.7	29.1 ± 0.3	0.43	1219 ± 13	367 ± 4
	24	5.8 ± 0.0	74.2 ± 0.6	36.7 ± 0.4	0.49	1960 ± 21	589 ± 6
IONCs@PEI	12	4.1 ± 0.1	42.0 ± 0.6	18.5 ± 0.7	0.44	680 ± 31	205 ± 9
	16	5.1 ± 0.0	52.6 ± 0.4	24.6 ± 0.4	0.47	1093 ± 67	329 ± 8
	24	7.2 ± 0.2	61.8 ± 0.4	33.1 ± 1.2	0.54	1906 ± 93	573 ± 28
AgNWs@IONCs@PEI	12	5.4 ± 0.3	27.4 ± 1.3	15.6 ± 1.2	0.57	599 ± 41	180 ± 12
	16	7.1 ± 0.8	35.2 ± 2.8	20.9 ± 2.1	0.59	1034 ± 121	311 ± 37
	24	13.1 ± 0.8	36.9 ± 1.5	34.1 ± 1.1	0.92	2245 ± 38	675 ± 11

at 300 kHz and magnetic field strengths of 12 and 16 kA m^{-1}, respectively. When the magnetic field strength was increased to 24 kA m^{-1}, the H_c values increased by 53%, 67%, and 82% at 110, 200, and 300 kHz, respectively. This increase in the H_c values of the AgNWs@IONCs@PEI sample resulted in the largest hysteresis loop area among all samples at 300 kHz and 24 kA m^{-1}. It was reported by Barrera *et al.* that strong dipolar interactions between nanoparticles, like in a chain configuration, can increase the overall energy barrier, making the coercive field much larger than the vertex field (Fig. 5a–c).[18]

Another essential characteristic of the hysteresis loops that provide details on the interactions of the magnetic particles is the reduced remanent magnetization M_r/M_s. Fig. 5d–f show the graphs of M_r/M_s values at various frequencies depending on the applied magnetic field intensity. The ratio of M_r/M_s equals 0.5 for a system of single-domain particles that do not interact with each other, according to the Stoner–Wohlfarth model.[84] Any deviation from this ratio provides information about particle interactions. If this ratio is less than 0.5, the decrease may be attributed to the dipolar interactions of randomly oriented nanoparticles; on the other hand, if the ratio is greater than 0.5, magnetic coupling may be indicated, as in the case of chain arrangement. It was observed that by increasing the applied H_{AC} to 24 kA m^{-1}, the M_r/M_s values of AgNWs@IONCs@PEI reached 0.67, 0.79, and 0.92 for frequencies of 110, 200, and 300 kHz, respectively, whereas the M_r/M_s value of the IONCs@PEI sample was around 0.50 for the same magnetic field conditions.

Fig. 5g, 5h, and 5i show that the SAR values of IONCs@COOH, IONCs@PEI, and AgNWs@IONCs@PEI increase with increasing frequency and magnetic field strength. The SAR values of AgNWs@IONCs@PEI were 29% and 8% lower than those of IONCs@PEI at 110 kHz, 28% and 10% lower at 200 kHz, and 12% and 5% lower at 300 kHz at magnetic field strengths of 12 and 16 kA m^{-1}, respectively. When the magnetic field strength was increased to 24 kA m^{-1}, the SAR values of AgNWs@IONCs@PEI increased by 16% at 110 kHz and 18% at 200 and 300 kHz compared to IONCs@PEI, exhibiting the highest SAR among all samples at all applied frequencies. Fig. 5a–c and g–i show that at 24 kA m^{-1}, single nanoparticles and aligned nanoparticles exhibit different magnetic properties under a dynamic magnetic field at all applied frequencies. Although the AgNWs@IONCs@PEI sample is not perfectly aligned, the magnetic properties change with the assembly of nanoparticles.

It was observed that, regardless of the applied field frequency, dipolar coupling between the magnetic moments of the nanoparticles in the AgNWs@IONCs@PEI sample was sustained at 24 kA m^{-1}. However, TEM images revealed that the IONCs@PEI particles were not perfectly aligned along the AgNWs and exhibited localized clustering and gaps between the chains. Previous studies have reported that increased interparticle spacing and the formation of incomplete chains weaken dipolar interactions, while antiparallel or out-of-plane coupling between chains reduces overall anisotropy and consequently lowers the SAR value.[15,87,88] Therefore, the applied
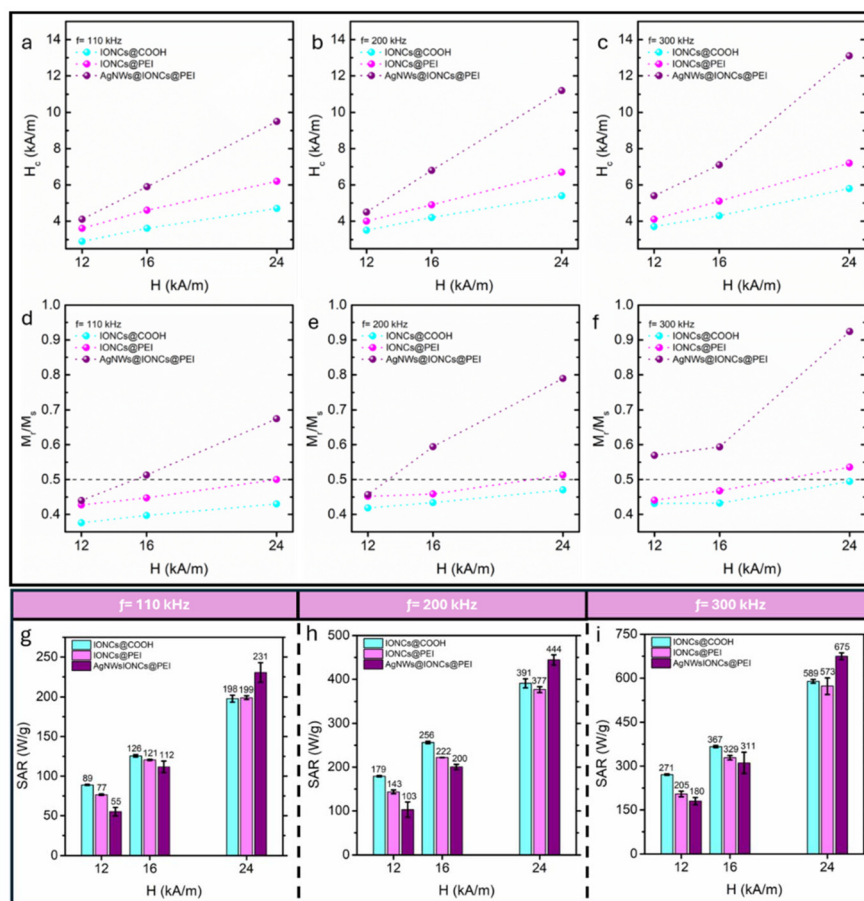
Fig. 5 Evaluation of H_c (a–c) and M_s/M_r (d–f) values as a function of applied magnetic field strength at various frequencies. The SAR values of IONCs@COOH, IONCs@PEI, and AgNWs@IONCs@PEI at various magnetic field strengths and frequencies of 110 (g), 200 (h), and 300 kHz (i).

magnetic field strengths of 12 and 16 kA m^{-1} may have been insufficient to induce a chain-like structure.

The dependence of the SAR value on f and H_{AC} has been shown in the literature theoretically and experimentally.[7,14] The area of the hysteresis curve increased with increasing H_{AC}, and the highest SAR value was obtained at 300 kHz and 24 kA m^{-1} for all samples, as expected. Alphandéry *et al.* reported similar observations regarding the effect of magnetic field strength on SAR values. The SAR of magnetosome chains increased from 864 to 1242 W g$^{-1}_{Fe}$ as the field strength rose from 18 to kA m^{-1} at 108 kHz.[89] Niculaes *et al.* also observed a similar increasing trend in SAR values when the magnetic field strength was raised from 24 to 48 kA m^{-1} at 300 kHz.[15] Generally, the SAR value is proportional to the square of the H_{AC}. The effect of frequency is more complex than H_{AC}: indeed, hysteresis losses increase with increasing frequency because, at higher frequencies, the magnetic domains have less time to reorient themselves in response to the changing magnetic field. As a result, more energy is dissipated as heat. For example, as shown in Table 1, the SAR of AgNWs@IONCs@PEI at 24 kA m^{-1} increased by 92% (from 231 ± 12 to 444 ± 12 W g$^{-1}_{Fe}$) as the frequency increased from

110 kHz to 200 kHz, and by 52% (from 444 ± 12 to 675 ± 11 W g$^{-1}_{Fe}$) as the frequency increased from 200 kHz to 300 kHz. It is worth noting that the AgNWs@IONCs@PEI sample had the highest SAR value when a field of 24 kA m^{-1} is applied throughout all the frequencies.

A one-way ANOVA and Tukey's *post-hoc* (Tables S2, S3 and S4) test was performed to assess whether there were statistically significant differences between the SAR and H_c values of the IONCs@COOH, IONCs@PEI, and AgNWs@IONCs@PEI samples. The results were considered statistically significant when $p < 0.05$. Tables S2 and S3 show that the observed SAR values of AgNWs@IONCs@PEI under a magnetic field strength of 24 kA m^{-1} were statistically significantly different from those of IONCs@COOH and IONCs@PEI, regardless of the applied frequency. Also, for H_c values (Table S4) recorded under all applied magnetic field conditions, except for 110 and 200 kHz frequencies with a field strength of 12 kA m^{-1}, the data were statistically significantly different from each other.

Additionally, to further confirm that the enhancement of H_c and SAR values arises from the electrostatic binding of IONCs@PEI to the AgNW surfaces and the subsequent for-

mation of chain-like structures, similar AC magnetometry experiments were conducted using IONCs@citrate nanoparticles, which exhibit a negative surface zeta potential and therefore are not capable of electrostatically interacting with the AgNW surfaces. For this purpose, a ligand exchange was carried out on oleic acid-capped IONCs by replacing the oleic acid with citrate molecules, providing a surface charge of 21 ± 2 mV and also enabling their effective water transfer (see the SI for the detailed protocol). Subsequently, AgNWs were mixed with IONCs@citrate at the same concentrations used for the AC magnetometry experiment with positively charged IONCs@PEI (0.6 mg_{Ag} mL^{-1} and 0.15 mg_{Fe} mL^{-1}). However, the sample was not washed to retain the non-attached IONCs@citrate in the sample. The AC hysteresis loops for IONCs@citrate nanoparticles alone and for AgNWs + IONCs@citrate are presented in Fig. S11, while one-way ANOVA analyses of the H_c and SAR values are given in Tables S5 and S6, respectively. The H_c results indicate that when there is no electrostatic interaction between the AgNWs and IONC particles and the IONCs do not form chain-like structures, no increase in the H_c field is observed for AgNWs + IONCs@citrate compared to IONCs@citrate, while a decrease in the SAR values is observed relative to IONCs@citrate. TEM images of the mixed sample of AgNWs with IONCs@citrate (AgNWs + IONCs@citrate) further confirm the lack of assembly of IONCs at the surface of the AgNWs (Fig. S10).

To assess the stability of the AgNWs@IONCs@PEI composites upon exposure to AMF, magnetic hyperthermia experiments were performed by exposing the AgNWs@IONCs@PEI composites to an AMF under high-field conditions and prolonged exposure (3 cycles of AMF of 30 minutes each). AgNWs@IONCs@PEI exhibited a gradual temperature increase of approximately 4 °C during the first 30 min, reaching nearly 28 °C by the end of each cycle (Fig. S12a). However, the differences in heating rate between the first and third cycles are attributed to the progressively higher initial temperature of the dispersion in each subsequent cycle. At the same time, the colloidal and morphological stability of AgNWs@IONCs@PEI also confirmed the presence of well-coated AgNWs with IONCs@PEI as an indication of a stable AgNWs@IONCs@PEI sample configuration (Fig. S12b–e). By visual inspection, the vial before AMF exposure showed homogeneous dispersions, while after 30 min of AMF exposure, partial precipitation was observed. This instability was, however, only temporary, and upon shaking the sample solution turned homogeneous again.

The strength of magnetic dipolar coupling depends on the distance between magnetic nanoparticles and the applied magnetic field strength.[16] Low magnetic field strengths may not be sufficient to form stable chain-like structures, and the nanoparticles may remain randomly dispersed. At higher field strengths, dipolar interactions become stronger and promote the formation of chain-like structures. The magnetic moments of the nanoparticles align with the field, and the dipolar forces between them pull the particles together into chains or columns. It can be concluded that the magnetic nanoparticles

in the AgNWs@IONCs@PEI sample are anisotropically arranged in chains or columns at 24 kA m^{-1}, and the resulting dipolar interactions increase uniaxial anisotropy, leading to collective magnetization behavior and resulting in the formation of a higher coercive field.[7] The H_{AC}-dependent chain formation explains the high SAR values obtained at a magnetic field intensity of 24 kA m^{-1} for the AgNWs@IONCs@PEI sample. According to Morales *et al.*, the larger the H_{AC}, the more pronounced the chain formation is by many chains or long chains.[84] The anisotropic arrangement of magnetic nanoparticles increases the overall energy barrier, resulting in a higher coercive field and an enlarged hysteresis loop area, thereby enhancing heat dissipation. Consequently, the formation of chain or column-like anisotropic structures at 24 kA m^{-1} in the AgNWs@IONCs@PEI sample led to a higher coercive field and, accordingly, an increased SAR value in the present study.[15,89]

In addition, TEM analysis was performed on the AgNWs@IONCs@PEI sample after the AC magnetometry measurements, and images before and after the analysis are given in Fig. S13. It can be concluded that IONCs were successfully immobilized on the surface of AgNWs. Thus, the assemblies on the template were largely preserved even after AC magnetometer measurements.

Conclusions

IONCs were successfully assembled into chain-like structures on the surfaces of micrometer-sized AgNWs. The high aspect ratio of AgNWs enables long-range ordering of IONCs@PEI clusters. Overall, our findings confirm that electrostatic interactions, when attractive, play a crucial role in the formation of chain-like structures by attracting oppositely charged IONCs and driving self-assembly.

The heating efficiency of the nanostructures determined by AC magnetometry analysis and the corresponding SAR values showed that the AgNWs@IONCs@PEI sample had the highest SAR values when the applied magnetic field strength was increased to 24 kA m^{-1}, regardless of the field frequency. The M_s, H_c, and M_r/M_s data extracted from the dynamic hysteresis loop show that the dipole coupling of the magnetic moments can be promoted at 24 kA m^{-1} under these experimental conditions. Lower fields (*i.e.*, 12 and 16 kA m^{-1}) were insufficient to excite the chain-like structure of AgNWs@IONCs@PEI, leading to lower SAR values, most likely due to the antiparallel alignment of the magnetic moments of the nanoparticles. In addition, due to the immobilization of IONCs@PEI on AgNWs, the chain-like structures were retained when the magnetic field was removed.

Conflicts of interest

There are no conflicts to declare.

Data availability

The data supporting this article have been included as part of the supplementary information (SI) and in the main paper and original figures and data files can be requested directly from the authors of this work. Supplementary information is available. The SI reports detailed SEM and TEM characterizations, along with schematics of the functionalization procedures for AgNWs, IONCs, and hybrid nanocomposites. It includes stability tests in aqueous and biological media, as well as assessments of magnetic response and heating performance under an AMF. AC magnetometry data, hysteresis loops, and pre- and post-AMF imaging are presented. Statistical analyses (ANOVA and Tukey tests) of magnetic parameters and SAR values across all samples are also included. See DOI: https://doi.org/10.1039/d5nr03252k.

Acknowledgements

References

1 C. L. Dennis and R. Ivkov, Physics of Heat Generation Using Magnetic Nanoparticles for Hyperthermia, *Int. J. Hyperthermia*, 2013, **29**(8), 715–729, DOI: 10.3109/02656736.2013.836758.

2 V. V. Mody, A. Singh and B. Wesley, Basics of Magnetic Nanoparticles for Their Application in the Field of Magnetic Fluid Hyperthermia, *Eur. J. Nanomed.*, 2013, **5**(1), 11–21, DOI: 10.1515/ejnm-2012-0008.

3 H. Gavilán, S. K. Avugadda, T. Fernández-Cabada, N. Soni, M. Cassani, B. T. Mai, R. Chantrell and T. Pellegrino, Magnetic Nanoparticles and Clusters for Magnetic Hyperthermia: Optimizing Their Heat Performance and Developing Combinatorial Therapies to Tackle Cancer, *Chem. Soc. Rev.*, 2021, **50**(20), 11614–11667, DOI: 10.1039/D1CS00427A.

4 M. P. Calatayud, E. Soler, T. E. Torres, E. Campos-Gonzalez, C. Junquera, M. R. Ibarra and G. F. Goya, Cell Damage Produced by Magnetic Fluid Hyperthermia on Microglial BV2 Cells, *Sci. Rep.*, 2017, **7**(1), 8627, DOI: 10.1038/s41598-017-09059-7.

5 B. T. Mai, T. Fernandez-Cabada, J. S. Conteh, G. E. P. Nucci, S. Fiorito, H. Gavilán, D. Debellis, L. Gjurgjaj and T. Pellegrino, Nanoplatforms for Magnetic–Photo–Heating of Thermo–Resistant Tumor Cells: Singular Synergic Therapeutic Effects at Mild Temperature, *Small*, 2024, **20**(51), 2310522, DOI: 10.1002/smll.202310522.

6 A. J. Giustini, A. A. Petryk, S. M. Cassim, J. A. Tate, I. Baker and P. J. Hoopes, Magnetic Nanoparticle Hyperthermia in Cancer Treatment, *Nano LIFE*, 2010, **1**(1–2), 17–32, DOI: 10.1142/S1793984410000067.

7 A. E. Deatsch and E. E. Evans, Heating Efficiency in Magnetic Nanoparticle Hyperthermia, *J. Magn. Magn. Mater.*, 2014, **354**, 163–172, DOI: 10.1016/j.jmmm.2013.11.006.

8 H. Gavilán, K. Simeonidis, E. Myrovali, E. Mazarío, O. Chubykalo-Fesenko, R. Chantrell, L. Balcells, M. Angelakeris, M. P. Morales and D. Serantes, How Size, Shape and Assembly of Magnetic Nanoparticles Give Rise to Different Hyperthermia Scenarios, *Nanoscale*, 2021, **13**(37), 15631–15646, DOI: 10.1039/D1NR03484G.

9 Z. Nemati, J. Alonso, I. Rodrigo, R. Das, E. Garaio, J. Á García, I. Orue, M.-H. Phan and H. Srikanth, Improving the Heating Efficiency of Iron Oxide Nanoparticles by Tuning Their Shape and Size, *J. Phys. Chem. C*, 2018, **122**(4), 2367–2381, DOI: 10.1021/acs.jpcc.7b10528.

10 Z. Ma, J. Mohapatra, K. Wei, J. P. Liu and S. Sun, Magnetic Nanoparticles: Synthesis, Anisotropy, and Applications, *Chem. Rev.*, 2023, **123**(7), 3904–3943, DOI: 10.1021/acs.chemrev.1c00860.

11 N. Silvestri, H. Gavilán, P. Guardia, R. Brescia, S. Fernandes, A. C. S. Samia, F. J. Teran and T. Pellegrino, Di- and Tri-Component Spinel Ferrite Nanocubes: Synthesis and Their Comparative Characterization for Theranostic Applications, *Nanoscale*, 2021, **13**(32), 13665–13680, DOI: 10.1039/D1NR01044A.

12 V. K. Chugh, S. Liang, D. Tonini, R. Saha, J. Liu, P. Yari, V. D. Krishna, M. C.-J. Cheeran, K. Wu and J.-P. Wang, Static and Dynamic Magnetization Responses of Self-Assembled Magnetic Nanoparticle Chains, *J. Phys. Chem. C*, 2023, **127**(37), 18494–18505, DOI: 10.1021/acs.jpcc.3c03755.

13 I. Morales, R. Costo, N. Mille, J. Carrey, A. Hernando and P. de la Presa, Time-Dependent AC Magnetometry and Chain Formation in Magnetite: The Influence of Particle Size, Initial Temperature and the Shortening of the Relaxation Time by the Applied Field, *Nanoscale Adv.*, 2021, **3**(20), 5801–5812, DOI: 10.1039/D1NA00463H.

14 E. Myrovali, K. Papadopoulos, I. Iglesias, M. Spasova, M. Farle, U. Wiedwald and M. Angelakeris, Long-Range Ordering Effects in Magnetic Nanoparticles, *ACS Appl. Mater. Interfaces*, 2021, **13**(18), 21602–21612, DOI: 10.1021/acsami.1c01820.

15 D. Niculaes, A. Lak, G. C. Anyfantis, S. Marras, O. Laslett, S. K. Avugadda, M. Cassani, D. Serantes, O. Hovorka, R. Chantrell and T. Pellegrino, Asymmetric Assembling of Iron Oxide Nanocubes for Improving Magnetic Hyperthermia Performance, *ACS Nano*, 2017, **11**(12), 12121–12133, DOI: 10.1021/acsnano.7b05182.

16 S. V. Komogortsev, V. A. Fel'k and O. A. Li, The Magnetic Dipole-Dipole Interaction Effect on the Magnetic Hysteresis at Zero Temperature in Nanoparticles Randomly Dispersed within a Plane, *J. Magn. Magn. Mater.*, 2019, **473**, 410–415, DOI: 10.1016/j.jmmm.2018.10.091.

17 C. Martinez-Boubeta, K. Simeonidis, A. Makridis, M. Angelakeris, O. Iglesias, P. Guardia, A. Cabot, L. Yedra, S. Estradé, F. Peiró, Z. Saghi, P. A. Midgley, I. Conde-Leborán, D. Serantes and D. Baldomir, Learning from Nature to Improve the Heat Generation of Iron-Oxide Nanoparticles for Magnetic Hyperthermia Applications, *Sci. Rep.*, 2013, **3**(1), 1652, DOI: 10.1038/srep01652.

18 G. Barrera, P. Allia and P. Tiberto, Dipolar Interactions among Magnetite Nanoparticles for Magnetic Hyperthermia: A Rate-Equation Approach, *Nanoscale*, 2021, **13**(7), 4103–4121, DOI: 10.1039/D0NR07397K.

19 J. G. Ovejero, F. Spizzo, M. P. Morales and L. Del Bianco, Nanoparticles for Magnetic Heating: When Two (or More) Is Better Than One, *Materials*, 2021, **14**(21), 6416, DOI: 10.3390/ma14216416.

20 T. Raczka, L. Luthardt, S. Müssig, N. Kent, Q. Lan, T. Denneulin, R. E. Dunin-Borkowski and K. Mandel, Magnetically "Programming" Cobalt–Doped Iron Oxide Nanoparticles for Localized Induction Heating: Triggering a Collective Effect of Magnetic Moment Alignment on Demand, *Adv. Mater.*, 2025, **37**(40), DOI: 10.1002/adma.202507158.

21 J. M. Orozco-Henao, D. F. Coral, D. Muraca, O. Moscoso-Londoño, P. Mendoza Zélis, M. B. Fernandez van Raap, S. K. Sharma, K. R. Pirota and M. Knobel, Effects of Nanostructure and Dipolar Interactions on Magnetohyperthermia in Iron Oxide Nanoparticles, *The Journal of Physical Chemistry C*, 2016, **120**(23), 12796–12809, DOI: 10.1021/acs.jpcc.6b00900.

22 B. L. Zambrano, C. Forró, E. Poloni, R. Hennig, P. Sivananthaguru, A. F. Renz, A. R. Studart and J. Vörös, Magnetic Manipulation of Nanowires for Engineered Stretchable Electronics, *ACS Nano*, 2022, **16**(1), 837–846, DOI: 10.1021/acsnano.1c08381.

23 M. H. Rizvi, R. Wang, J. Schubert, W. D. Crumpler, C. Rossner, A. L. Oldenburg, A. Fery and J. B. Tracy, Magnetic Alignment for Plasmonic Control of Gold Nanorods Coated with Iron Oxide Nanoparticles, *Adv. Mater.*, 2022, **34**(40), 2203366, DOI: 10.1002/adma.202203366.

24 H. Mok and M. Zhang, Superparamagnetic iron oxide nanoparticle-based delivery systems for biotherapeutics, *Expert Opin. Drug Delivery*, 2013, **10**(1), 73–87, DOI: 10.1517/17425247.2013.747507.

25 A. Gole, J. W. Stone, W. R. Gemmill, H.-C. zur Loye and C. J. Murphy, Iron Oxide Coated Gold Nanorods: Synthesis, Characterization, and Magnetic Manipulation, *Langmuir*, 2008, **24**(12), 6232–6237, DOI: 10.1021/la703975y.

26 B. Zhang, Q. Yu and Y. Liu, Polarization of Stem Cells Directed by Magnetic Field-Manipulated Supramolecular Polymeric Nanofibers, *ACS Appl. Mater. Interfaces*, 2021, **13**(8), 9580–9588, DOI: 10.1021/acsami.0c19428.

27 L. Hein and S. Coulombe, Synthesis and Characterization of Magnetic Nanoparticle-Decorated Multiwalled Carbon Nanotubes, *ACS Omega*, 2024, **9**(38), 39776–39791, DOI: 10.1021/acsomega.4c05027.

28 D. Guo, X. Ji, H. Wang, B. Sun, B. Chu, Y. Shi, Y. Su and Y. He, Silicon Nanowire-Based Multifunctional Platform for Chemo-Photothermal Synergistic Cancer Therapy, *J. Mater. Chem. B*, 2018, **6**(23), 3876–3883, DOI: 10.1039/c7tb02907a.

29 B. Azeredo, A. Carton, C. Leuvrey, C. Kiefer, D. Ihawakrim, S. Zafairatos, M. Gallart, P. Gilliot and B. P. Pichon, Synergistic Photo Optical and Magnetic Properties of a Hybrid Nanocomposite Consisting of a Zinc Oxide Nanorod Array Decorated with Iron Oxide Nanoparticles, *J. Mater. Chem. C*, 2018, **6**(39), 10502–10512, DOI: 10.1039/C8TC02680G.

30 Z. Wang, B. Jiao, Y. Qing, H. Nan, L. Huang, W. Wei, Y. Peng, F. Yuan, H. Dong, X. Hou and Z. Wu, Flexible and Transparent Ferroferric Oxide-Modified Silver Nanowire Film for Efficient Electromagnetic Interference Shielding, *ACS Appl. Mater. Interfaces*, 2020, **12**(2), 2826–2834, DOI: 10.1021/acsami.9b17513.

31 D. Beketova, M. Motola, H. Sopha, J. Michalicka, V. Cicmancova, F. Dvorak, L. Hromadko, B. Frumarova, M. Stoica and J. M. Macak, One-Step Decoration of TiO2 Nanotubes with Fe3O4 Nanoparticles: Synthesis and Photocatalytic and Magnetic Properties, *ACS Appl. Nano Mater.*, 2020, **3**(2), 1553–1563, DOI: 10.1021/acsanm.9b02337.

32 W.-C. Wu, Q. Li, N. Holten-Andersen and J. B. Tracy, Heteroaggregation Approach for Depositing Magnetite Nanoparticles onto Silica-Overcoated Gold Nanorods, *Chem. Mater.*, 2017, **29**(24), 10362–10368, DOI: 10.1021/acs.chemmater.7b03481.

33 Z. Wang, J. Zhu, H. Wang, W. Chen, Q. Yan, J. Zhang and Y. Chen, Synthesis and magnetic properties of nickel nano-particles deposited on the silicon nanowires, *J. Alloys Compd.*, 2012, **511**(1), 257–261, DOI: 10.1016/j.jallcom.2011.09.047.

34 N. Li, G.-W. Huang, X.-J. Shen, H.-M. Xiao and S.-Y. Fu, Controllable Fabrication and Magnetic-Field Assisted Alignment of Fe3O4-Coated Ag Nanowires via a Facile Co-Precipitation Method, *J. Mater. Chem. C*, 2013, **1**(32), 4879, DOI: 10.1039/c3tc30270a.

35 N. Li, G.-W. Huang, H.-M. Xiao and S.-Y. Fu, Preparation of Aligned Fe3O4@Ag-Nanowire/Poly(Vinyl Alcohol) Nanocomposite Films via a Low Magnetic Field, *Composites, Part A*, 2015, **77**, 87–95, DOI: 10.1016/j.compositesa.2015.06.019.

36 H. Geng, D. Ge, S. Lu, J. Wang, Z. Ye, Y. Yang, J. Zheng and H. Gu, Preparation of a Γ–Fe2O3/Ag Nanowire Coaxial Nanocable for High–Performance Lithium–Ion Batteries, *Chem. – Eur. J.*, 2015, **21**(31), 11129–11133.

37 H. Liu, D. Wei, Y. Yan, A. Li, X. Chuai, G. Lu and Y. Wang, Silver Nanowire Templating Synthesis of Mesoporous SnO₂ Nanotubes: An Effective Gas Sensor for Methanol with a Rapid Response and Recovery, *ChemistrySelect*, 2018, **3**(27), 7741–7748, DOI: 10.1002/slct.201801663.

38 Y. Cao, J. He and J. Sun, Fabrication of Oriented Arrays of Porous Gold Microsheaths Using Aligned Silver Nanowires as Sacrificial Template, *Mater. Lett.*, 2009, **63**(1), 148–150, DOI: 10.1016/j.matlet.2008.09.026.

39 Z. Fu, L. Wang, W. Hu, Y. Zhou and Q. Zhou, Photoresponsive Silver Nanowire Nanoplatform for Real-Time Drug Delivery in Non-Small Cell Lung Cancer Therapy, *J. Indian Chem. Soc.*, 2024, **101**(9), 101239, DOI: 10.1016/j.jics.2024.101239.

40 Z. Chen, G. Liu, X. Zhang, J. Sui, X. Dong, W. Yu and C. Song, Synthesis of Multifunctional Rare-Earth Fluoride/Ag Nanowire Nanocomposite for Efficient Therapy of Cancer, *Mater. Sci. Eng., C*, 2019, **104**, 109940, DOI: 10.1016/j.msec.2019.109940.

41 L. Yang and Z. Huang, Three As-Synthesized Silver Nanowires (Ag NWs) with Different Size on Renal Cancer Treatment, *Mater. Express*, 2023, **13**(8), 1321–1325, DOI: 10.1166/mex.2023.2477.

42 I. G. Theodorou, K. H. Müller, S. Chen, A. E. Goode, V. Yufit, M. P. Ryan and A. E. Porter, Silver Nanowire Particle Reactivity with Human Monocyte-Derived Macrophage Cells: Intracellular Availability of Silver Governs Their Cytotoxicity, *ACS Biomater. Sci. Eng.*, 2017, **3**(10), 2336–2347, DOI: 10.1021/acsbiomaterials.7b00479.

43 F. Wang, Y. Wang, G. Qu, X. Yao, C. Ma, M. Song, H. Wang and G. Jiang, Ultralong AgNWs-Induced Toxicity in A549 Cells and the Important Roles of ROS and Autophagy, *Ecotoxicol. Environ. Saf.*, 2019, **186**, 109742, DOI: 10.1016/j.ecoenv.2019.109742.

44 L. Steinmetz, C. Geers, S. Balog, M. Bonmarin, L. Rodriguez-Lorenzo, P. Taladriz-Blanco, B. Rothen-Rutishauser and A. Petri-Fink, A Comparative Study of Silver Nanoparticle Dissolution under Physiological Conditions, *Nanoscale Adv.*, 2020, **2**(12), 5760–5768, DOI: 10.1039/D0NA00733A.

45 C. Liu, W. Leng and P. J. Vikesland, Controlled Evaluation of the Impacts of Surface Coatings on Silver Nanoparticle Dissolution Rates, *Environ. Sci. Technol.*, 2018, **52**(5), 2726–2734, DOI: 10.1021/acs.est.7b05622.

46 M. J. Kim and S. Shin, Toxic Effects of Silver Nanoparticles and Nanowires on Erythrocyte Rheology, *Food Chem. Toxicol.*, 2014, **67**, 80–86, DOI: 10.1016/j.fct.2014.02.006.

47 R. S. Jones, R. R. Draheim and M. Roldo, Silver Nanowires: Synthesis, Antibacterial Activity and Biomedical Applications, *Appl. Sci.*, 2018, **8**(5), 673.

48 S. Jiang and C. P. Teng, Fabrication of Silver Nanowires-Loaded Polydimethylsiloxane Film with Antimicrobial Activities and Cell Compatibility, *Mater. Sci. Eng., C*, 2017, **70**, 1011–1017, DOI: 10.1016/j.msec.2016.04.094.

49 F. Wang, Y. Wang, X. Yao, C. Ma, Y. Yin and M. Song, Length and Diameter-Dependent Phagocytosis and Cytotoxicity of Long Silver Nanowires in Macrophages, *Chemosphere*, 2019, **237**, 124565, DOI: 10.1016/j.chemosphere.2019.124565.

50 A. Schinwald, T. Chernova and K. Donaldson, Use of Silver Nanowires to Determine Thresholds for Fibre Length-Dependent Pulmonary Inflammation and Inhibition of Macrophage Migration in Vitro, *Part. Fibre Toxicol.*, 2012, **9**(1), 47, DOI: 10.1186/1743-8977-9-47.

51 Z. Šimonová, L. Porubová, A. Verner, R. Gabor, Z. Vilamová, E. Dobročka, M. Cieslar, V. Krbečková, K. P. Dědková, L. Svoboda, J. Bednář, R. Dvorský and J. Seidlerová, Simple Fabrication of Polycaprolactone-Co-Lactide Membrane with Silver Nanowires: Synthesis, Characterization and Cytotoxicity Studies, *Fibers Polym.*, 2022, **23**(11), 2983, DOI: 10.1007/s12221-022-4994-2.

52 Y. Li and W.-X. Wang, Uptake, Intracellular Dissolution, and Cytotoxicity of Silver Nanowires in Cell Models, *Chemosphere*, 2021, **281**, 130762, DOI: 10.1016/j.chemosphere.2021.130762.

53 J. Zhao, W. Xu, Z. Zhao, G. Ling and P. Zhang, Intelligent Nanocomposite Hydrogels with Simultaneous Photothermal Antitumor and Antibacterial Efficacy for Cutaneous Melanoma Treatment, *Composites, Part B*, 2022, **243**, 110130, DOI: 10.1016/j.compositesb.2022.110130.

54 Z. Wu, H. Zhuang, B. Ma, Y. Xiao, B. Koc, Y. Zhu and C. Wu, Manganese-Doped Calcium Silicate Nanowire Composite Hydrogels for Melanoma Treatment and Wound Healing, *Research*, 2021, **2021**, 9780943, DOI: 10.34133/2021/9780943.

55 J. Ma, W. Kai and M. Zhan, Growth Mechanism and Electrical and Magnetic Properties of Ag–Fe$_3$O$_4$ Core–Shell Nanowires, *ACS Appl. Mater. Interfaces*, 2015, **7**(29), 16027–16039, DOI: 10.1021/acsami.5b04342.

56 Z. Wang, B. Jiao, Y. Qing, H. Nan, L. Huang, W. Wei, Y. Peng, F. Yuan, H. Dong, X. Hou and Z. Wu, Flexible and Transparent Ferroferric Oxide-Modified Silver Nanowire Film for Efficient Electromagnetic Interference Shielding, *ACS Appl. Mater. Interfaces*, 2020, **12**(2), 2826–2834, DOI: 10.1021/acsami.9b17513.

57 O. Trotsenko, A. Tokarev, A. Gruzd, T. Enright and S. Minko, Magnetic Field Assisted Assembly of Highly Ordered Percolated Nanostructures and Their Application for Transparent Conductive Thin Films, *Nanoscale*, 2015, **7**(16), 7155–7161, DOI: 10.1039/C5NR00154D.

58 R. Lei, H. Ni, R. Chen, H. Gu, B. Zhang and W. Zhan, Ag nanowire-modified 1D α-Fe$_2$O$_3$ nanotube arrays for photo-catalytic degradation of methylene blue, *J. Nanopart. Res.*, 2017, **19**, 378, DOI: 10.1007/s11051-017-4055-8.

59 C. Martins, C. Rolo, V. R. G. Chaco, L. C. J. Pereira, J. P. Borges, J. C. Silva, T. Vieira and P. I. P. Soares, Enhancing the magnetic properties of superparamagnetic iron oxide nanoparticles using hydrothermal treatment for magnetic hyperthermia application, *Mater. Adv.*, 2025, **6**, 1726–1743, DOI: 10.1039/D4MA01120A.

60 S. Sarisozen, N. A. Tertemiz, T. A. Arica, N. Polat, C. Kocabas, F. M. Balci and S. Balci, Transition Metal Salt Promoted, Green, and High–Yield Synthesis of Silver Nanowires for Flexible Transparent Conductive Electrodes, *ChemistrySelect*, 2021, **6**(44), 12548–12554.

61 H. Gavilán, G. M. R. Rizzo, N. Silvestri, B. T. Mai and T. Pellegrino, Scale-up Approach for the Preparation of

Magnetic Ferrite Nanocubes and Other Shapes with Benchmark Performance for Magnetic Hyperthermia Applications, *Nat. Protoc.*, 2023, **18**(3), 783–809, DOI: 10.1038/s41596-022-00779-3.

62 M. Cruz-Acuña, L. Maldonado-Camargo, J. Dobson and C. Rinaldi, From Oleic Acid-Capped Iron Oxide Nanoparticles to Polyethyleneimine-Coated Single-Particle Magnetofectins, *J. Nanopart. Res.*, 2016, **18**(9), 268, DOI: 10.1007/s11051-016-3577-9.

63 K. K. Narayanasamy, M. Cruz-Acuña, C. Rinaldi, J. Everett, J. Dobson and N. D. Telling, Alternating Current (AC) Susceptibility as a Particle-Focused Probe of Coating and Clustering Behaviour in Magnetic Nanoparticle Suspensions, *J. Colloid Interface Sci.*, 2018, **532**, 536–545, DOI: 10.1016/j.jcis.2018.08.014.

64 B. Wiley, Y. Sun and Y. Xia, Polyol Synthesis of Silver Nanostructures: Control of Product Morphology with Fe(II) or Fe(III) Species, *Langmuir*, 2005, **21**(18), 8077–8080, DOI: 10.1021/la050887i.

65 R. F. Hamans, M. Parente, A. Garcia-Etxarri and A. Baldi, Optical Properties of Colloidal Silver Nanowires, *J. Phys. Chem. C*, 2022, **126**(20), 8703–8709, DOI: 10.1021/acs.jpcc.2c01251.

66 F. Wu, L. Cheng and W. Wang, Surface Plasmon Resonance of Large-Size Ag Nanobars, *Micromachines*, 2022, **13**(4), 638, DOI: 10.3390/mi13040638.

67 T. Tomiyama and H. Yamazaki, Optical Anisotropy Studies of Silver Nanowire/Polymer Composite Films with Mueller Matrix Ellipsometry, *Appl. Surf. Sci.*, 2017, **421**, 831–836, DOI: 10.1016/j.apsusc.2017.01.152.

68 Z. Chen, Z. Lv, Y. Sun, Z. Chi and G. Qing, Recent Advancements in Polyethyleneimine-Based Materials and Their Biomedical, Biotechnology, and Biomaterial Applications, *J. Mater. Chem. B*, 2020, **8**(15), 2951–2973, DOI: 10.1039/C9TB02271F.

69 M. Gorohovs and Y. Dekhtyar, Surface Functionalization of Nanoparticles for Enhanced Electrostatic Adsorption of Biomolecules, *Molecules*, 2025, **30**(15), DOI: 10.3390/molecules30153206.

70 A. von Harpe, H. Petersen, Y. Li and T. Kissel, Characterization of Commercially Available and Synthesized Polyethylenimines for Gene Delivery, *J. Controlled Release*, 2000, **69**(2), 309–322, DOI: 10.1016/S0168-3659(00)00317-5.

71 M. Testa-Anta, M. A. Ramos-Docampo, M. Comesaña-Hermo, B. Rivas-Murias and V. Salgueiriño, Raman Spectroscopy to Unravel the Magnetic Properties of Iron Oxide Nanocrystals for Bio-Related Applications, *Nanoscale Adv.*, 2019, **1**(6), 2086–2103, DOI: 10.1039/C9NA00064J.

72 Y. Hadadian, H. Masoomi, A. Dinari, C. Ryu, S. Hwang, S. Kim, B. K. Cho, J. Y. Lee and J. Yoon, From Low to High Saturation Magnetization in Magnetite Nanoparticles: The Crucial Role of the Molar Ratios between the Chemicals, *ACS Omega*, 2022, **7**(18), 15996–16012, DOI: 10.1021/ACSOMEGA.2C01136/ASSET/IMAGES/LARGE/AO2C01136_0011.JPEGm.

73 C. M. Guvenc, N. Polat, T. A. Arica and S. Balci, Selective Growth of FAPbBr₃ Nanocrystals with Precisely Tailored Optical Properties for Advanced Optoelectronic Applications, *ACS Appl. Nano Mater.*, 2025, **8**(11), 5713–5720, DOI: 10.1021/acsanm.5c00246.

74 C. N. Dibenedetto, T. Sibillano, R. Brescia, M. Prato, L. Triggiani, C. Giannini, A. Panniello, M. Corricelli, R. Comparelli, C. Ingrosso, N. Depalo, A. Agostiano, M. L. Curri, M. Striccoli and E. Fanizza, PbS Quantum Dots Decorating TiO2 Nanocrystals: Synthesis, Topology, and Optical Properties of the Colloidal Hybrid Architecture, *Molecules*, 2020, **25**(12), 2939, DOI: 10.3390/molecules25122939.

75 R. Wang, Y. Hu, Y. Yang, W. Xu, M. Yao, D. Gao, Y. Zhao, S. Zhan, X. Shi and X. Wang, Using PEGylated Iron Oxide Nanoparticles with Ultrahigh Relaxivity for MR Imaging of an Orthotopic Model of Human Hepatocellular Carcinoma, *J. Nanopart. Res.*, 2017, **19**(2), 39, DOI: 10.1007/s11051-016-3718-1.

76 C. K. Choudhury and S. Roy, Structural and Dynamical Properties of Polyethylenimine in Explicit Water at Different Protonation States: A Molecular Dynamics Study, *Soft Matter*, 2013, **9**(7), 2269, DOI: 10.1039/c2sm26290h.

77 C. Balbuena, M. M. Gianetti and E. R. Soulé, Molecular Dynamics Simulations of the Formation of Ag Nanoparticles Assisted by PVP, *Phys. Chem. Chem. Phys.*, 2021, **23**(11), 6677–6684, DOI: 10.1039/D1CP00211B.

78 A. Sharonova, K. Loza, M. Surmeneva, R. Surmenev, O. Prymak and M. Epple, Synthesis of Positively and Negatively Charged Silver Nanoparticles and Their Deposition on the Surface of Titanium, *IOP Conf. Ser.: Mater. Sci. Eng.*, 2016, **116**, 012009, DOI: 10.1088/1757-899X/116/1/012009.

79 A. Krieger, A. Zika and F. Gröhn, Functional Nano-Objects by Electrostatic Self-Assembly: Structure, Switching, and Photocatalysis, *Front. Chem.*, 2022, **9**, 1–46, DOI: 10.3389/fchem.2021.779360.

80 L. D. Scanlan, R. B. Reed, A. V. Loguinov, P. Antczak, A. Tagmount, S. Aloni, D. T. Nowinski, P. Luong, C. Tran, N. Karunaratne, D. Pham, X. X. Lin, F. Falciani, C. P. Higgins, J. F. Ranville, C. D. Vulpe and B. Gilbert, Silver Nanowire Exposure Results in Internalization and Toxicity to Daphnia Magna, *ACS Nano*, 2013, 7(12), 10681–10694, DOI: 10.1021/nn4034103.

81 C. Michaeloudes, J. Seiffert, S. Chen, P. Ruenraroengsak, L. Bey, I. G. Theodorou, M. Ryan, X. Cui, J. Zhang, M. Shaffer, T. Tetley, A. E. Porter and K. F. Chung, Effect of Silver Nanospheres and Nanowires on Human Airway Smooth Muscle Cells: Role of Sulfidation, *Nanoscale Adv.*, 2020, **2**(12), 5635–5647, DOI: 10.1039/D0NA00745E.

82 S. G. Lehmann, D. Toybou, A.-E. P. del Real, D. Arndt, A. Tagmount, M. Viau, M. Safi, A. Pacureanu, P. Cloetens, S. Bohic, M. Salomé, H. Castillo-Michel, B. Omaña-Sanz, A. Hofmann, C. Vulpe, J.-P. Simonato, C. Celle, L. Charlet and B. Gilbert, Crumpling of Silver Nanowires by Endolysosomes Strongly Reduces Toxicity, *Proc. Natl. Acad.*

Sci. U. S. A., 2019, **116**(30), 14893–14898, DOI: 10.1073/pnas.1820041116.

83 S. Dutz, R. Hergt, J. Mürbe, R. Müller, M. Zeisberger, W. Andrä, J. Töpfer and M. E. Bellemann, Hysteresis Losses of Magnetic Nanoparticle Powders in the Single Domain Size Range, *J. Magn. Magn. Mater.*, 2007, **308**(2), 305–312, DOI: 10.1016/j.jmmm.2006.06.005.

84 I. Morales, R. Costo, N. Mille, G. B. Da Silva, J. Carrey, A. Hernando and P. De la Presa, High Frequency Hysteresis Losses on γ-Fe2O3 and Fe3O4: Susceptibility as a Magnetic Stamp for Chain Formation, *Nanomaterials*, 2018, **8**(12), 970, DOI: 10.3390/nano8120970.

85 S. K. Avugadda, N. Soni, E. M. Rodrigues, S. Persano and T. Pellegrino, Protease-Mediated T_1 Contrast Enhancement of Multilayered Magneto-Gadolinium Nanostructures for Imaging and Magnetic Hyperthermia, *ACS Appl. Mater. Interfaces*, 2024, **16**(6), 6743–6755, DOI: 10.1021/acsami.3c13914.

86 T. Yamaminami, S. Ota, S. B. Trisnanto, M. Ishikawa, T. Yamada, T. Yoshida, K. Enpuku and Y. Takemura, Power Dissipation in Magnetic Nanoparticles Evaluated Using the AC Susceptibility of Their Linear and Nonlinear Responses, *J. Magn. Magn. Mater.*, 2021, **517**, 167401, DOI: 10.1016/j.jmmm.2020.167401.

87 D. Toulemon, M. V. Rastei, D. Schmool, J. S. Garitaonandia, L. Lezama, X. Cattoën, S. Bégin-Colin and B. P. Pichon, Enhanced Collective Magnetic Properties Induced by the Controlled Assembly of Iron Oxide Nanoparticles in Chains, *Adv. Funct. Mater.*, 2016, **26**(15), 2454–2462, DOI: 10.1002/adfm.201505086m.

88 S. K. Avugadda, M. E. Materia, R. Nigmatullin, D. Cabrera, R. Marotta, T. F. Cabada, E. Marcello, S. Nitti, E. J. Artés-Ibañez, P. Basnett, C. Wilhelm, F. J. Teran, I. Roy and T. Pellegrino, Esterase-Cleavable 2D Assemblies of Magnetic Iron Oxide Nanocubes: Exploiting Enzymatic Polymer Disassembling To Improve Magnetic Hyperthermia Heat Losses, *Chem. Mater.*, 2019, **31**(15), 5450–5463, DOI: 10.1021/acs.chemmater.9b00728.

89 E. Alphandéry, S. Faure, L. Raison, E. Duguet, P. A. Howse and D. A. Bazylinski, Heat Production by Bacterial Magnetosomes Exposed to an Oscillating Magnetic Field, *J. Phys. Chem. C*, 2011, **115**(1), 18–22, DOI: 10.1021/jp104580t.